THE JOURNAL OF PHYSICAL CHEMISTRY B

ARTICLE

pubs.acs.org/JPCB

Kinetics of Carbon Monoxide Migration and Binding in Solvated Neuroglobin As Revealed by Molecular Dynamics Simulations and Quantum Mechanical Calculations

Massimiliano Anselmi,*[,†] Alfredo Di Nola,[†] and Andrea Amadei[‡]

[†]Department of Chemistry, University of Rome "La Sapienza", Rome, Italy

[‡]Department of Chemistry, University of Rome "Tor Vergata", Rome, Italy

Supporting Information

ABSTRACT: Neuroglobin (Ngb) is a globular protein that reversibly binds small ligands at the six coordination position of the heme. With respect to other globins similar to myoglobin, Ngb displays some peculiarities as the topological reorganization of the internal cavities coupled to the sliding of the heme, or the binding of the endogenous distal histidine to the heme in the absence of an exogenous ligand. In this Article, by using multiple (independent) molecular dynamics trajectories (about 500 ns in total), the migration pathways of photolized carbon monoxide (CO) within solvated Ngb were analyzed, and a quantitative description of CO migration and corresponding kinetics was obtained. MD results, combined with quantum mechanical calculations on the CO−heme binding−unbinding reaction step in Ngb, allowed construction of a quantitative model representing the relevant steps of CO migration and rebinding.

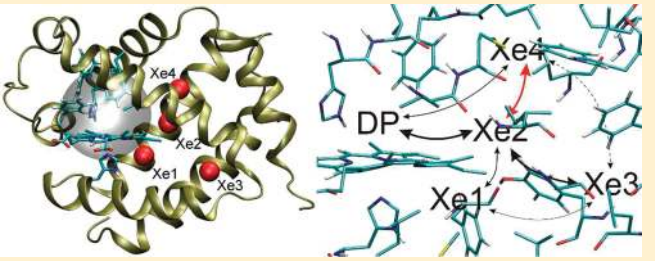

INTRODUCTION

The ligand diffusion in the interior of globins has been extensively investigated in recent years with several experimental and computational techniques. The major contribution for the knowledge of such a topic has come from the study of myoglobin (Mb). In fact, the small size, the relative structural stability, and the complex functional behavior make myoglobin a perfect model system to investigate, at the atomic level, protein biochemical activities. Time-resolved X-ray diffraction,[1−5] Fourier transform infrared spectroscopy,[6−9] kinetic measurements,[10,11] and theoretical approaches[12−18] are usefully adopted to study the diffusion of small diatomic ligands, such as O_2, CO, and NO, in wild-type Mbs and their mutants.

However, a few years ago, neuroglobin (Ngb), a new member of the globin family, was discovered to be markedly expressed in the brain.[19] Like Mb, Ngb is a monomeric protein, which reversibly binds small ligands at the sixth coordination position of the heme, and, despite its small sequence similarity with other globins, it displays the typical globin fold; consequently, Ngb conserves some canonical residues, among others a proximal histidine that steadily binds to the heme iron and a distal histidine facing the binding site.[20,21] In the ferrous form, Ngb binds O_2, CO, and NO, but, in contrast to Mb, in the absence of an exogenous ligand, both the ferric and the ferrous forms are hexacoordinated to the proximal and distal histidines.[22,23] Such a behavior implies a competition between an exogenous ligand and the distal histidine for the binding at the sixth coordination position on the heme.

The physiological role of Ngb is still unknown, even though convincing experimental evidence shows that it is involved in the regulation of a still unclear neuronal protective mechanism under hypoxia and ischemia.[24,25] Experimental observations show that Ngb interacts with the α-subunit of heterotrimeric $G_{\alpha\beta\gamma}$ protein, enforcing the hypothesis, which assigns to Ngb a role of signal transducer.[26−28] Recently, it has been suggested that Ngb inhibits the intrinsic pathway of apoptosis in vitro and may prevent the activation of pro-caspase 9 by interaction of cytochrome c.[29] Moreover, it is worth reminding that the average Ngb concentration seems too low (<1 μM) to play a Mb-like role in the transport and storage of O_2, although this function is not yet excluded.

Therefore, Ngb and Mb similarity makes such a protein an alternative and complementary system in the study of the globins, whereas its peculiarities represent a new challenge for the interpretation of the relation between structure and function. The three-dimensional structure was solved by X-ray diffraction for the unliganded Ngb from human and mouse[20,21] and for ferrous CO-bound Ngb.[30] Comparison of the crystal structures of two murine Ngb redox states[21,30] showed that binding of CO is associated to structural changes involving a significant heme sliding and a topological reorganization of the internal cavities.[30] Such a heme sliding was also detected with Molecular Dynamics

Received: November 12, 2010
Revised: January 17, 2011
Published: February 18, 2011

ACS Publications © 2011 American Chemical Society

(MD) simulations performed both in solution[31] and in the crystal environment.[32] Structural analysis demonstrated a topological analogy between the Ngb internal cavities[31] and the so-called Xe cavities detected in the interior of Mb.[33] Moreover, in Ngb, such cavities are coated principally by much conserved hydrophobic residues, which topologically correspond to those delimiting the Xe cavities in Mb,[31] and bind xenon or krypton atoms at high pressure.[34]

The relative placements of the Ngb cavities and such similarities with the Xe cavities have been confirmed from the study of the Ngb free energy landscape for O_2, CO, and NO.[35−37] However, the topological rearrangements occurring with the heme displacements (other than with structure fluctuations and redox state transformations) makes the motion of the photodissociated ligand through the Ngb cavity network an interesting process for elucidating how the evolution had selected the structure of the protein matrix to modulate the ligand affinity and diffusion. For that reason, the kinetics of ligand rebinding and the diffusion after photodissociation were studied at cryogenic and room temperature.[23,38]

In the present Article, we report the results of a theoretical/computational investigation of the kinetics of CO diffusion in murine Ngb after dissociation from heme. We performed 70 MD simulations (each 7.5 ns long) in solution that provided 70 independent trajectories of the CO migration in the protein. The time dependence of cavities occupancy, as obtained by MD simulations, was used to construct an explicit kinetic model, allowing us to obtain the kinetics of CO migration process within the nanoseconds time range.

METHODS

Considering the probable correlation between initial heme position and the escape rate of exogenous ligand from the binding site, the starting coordinates employed for the simulations were taken from the previously performed extended MD simulation of the CO-bound murine Ngb[31] in solution. We chose seven structures at times 10, 20, 28, 35, 45, 53, and 61 ns. After removing the stretching potential between heme iron and CO, we switched the heme geometry from hexacoordinated to pentacoordinated.[39] Thus, from the beginning of the simulations, the system was modeled as a reduced Ngb with a dissociated CO. Furthermore, for the whole length of the simulations, we considered the heme pentacoordinated, given that within a few nanoseconds both the CO recombination to the heme and the reaction between the heme and the endogenous ligand distal His could be neglected.[38] The CO molecule was modeled with the three-site "quadrupolar" CO model.[40] Note that more sophisticated CO models are nowadays available[16,41] involving fluctuating charges coupled to the intramolecular stretching coordinate or atomic multipoles. However, in this study, we employed the simpler three-site quadrupolar model, providing the essential features of carbon monoxide, to easily implement and integrate it in the force field, reproducing accurately the translational motion of CO. Before starting the production runs at 300 K, the initial configurations were minimized without restraints. For each configuration, we performed 10 independent simulations, starting from different sets of initial velocities, obtaining a total of 70 independent trajectories.

MD simulations were performed with the Gromacs software package[42] using the GROMOS96 force field.[43] Simulations were carried out at a constant temperature of 300 K within a fixed-volume rectangular box using periodic boundary conditions. The Lincs algorithm[44] to constrain all bond lengths and the roto-translational constraint algorithm[45] were used. The initial velocities were taken randomly from a Maxwellian distribution at 300 K, and the temperature was held constant by the isothermal algorithm.[46] The Particle Mesh Ewald (PME) method[47] was used for the calculation of the long-range interactions with a grid spacing of 0.12 nm combined with a fourth-order B-spline interpolation to compute the potential and forces in between grid points.[48] A nonbond pair list cutoff of 9.0 Å was used, and the pair list was updated every four time steps. A time step of 2 fs was used in all simulations.

We used the essential dynamics technique[49] to define the reaction coordinate describing the heme sliding.

The package SURFNET[50] was used for detecting the cavities and calculating their volumes. In this program, gap regions are defined by filling the empty regions in the interior of the molecule with gap spheres of variable radius (R_{min} = 1.0 Å and R_{max} = 3.0 Å, in our case). These spheres are then used to compute a 3D density map that, when contoured, defines the surface of the gap region. Cavity volumes were evaluated without taking into account the presence of the water and of CO. A cavity is considered "exposed" if the SURFNET program shows continuity between the cavity and the solvent.

All details on the Perturbed Matrix Method (PMM) theoretical framework and calculations as well as on the procedure employed to obtain the binding−unbinding kinetic rate constants can be found in previous papers.[51,52] The theoretical basis of PMM has been widely described elsewhere.[53,54] Here, only the main features of the computational strategy will be outlined. The underlying philosophy of PMM is essentially in line with all currently employed quantum mechanical/molecular mechanical (QM/MM) procedures.[55] A portion of a complex molecular system, hereafter called quantum center (QC), is treated quantum mechanically, with the rest of the system acting as a perturbation. Briefly, given the energies and dipole moments for ground and excited electronic states, which can be provided carrying out standard electronic structure calculations[56] on the isolated QC, it is possible to construct and diagonalize the perturbed Hamitonian matrix,[53,54] which considers the perturbation provided by the electric potential and field exerted by the environment. Because the perturbing field can be evaluated at each MD frame using the environment atomic charge distribution, a trajectory of the QC perturbed Hamiltonian eigenvalues and eigenvectors is obtained. Such calculations carried out along the reaction coordinate provide, within certain approximations, the reaction free energy and whatever electronic property at a generic reaction coordinate position.[57] Once the unperturbed energy profile for the reaction of CO binding−unbinding to heme is obtained,[51] the corresponding perturbed energy profiles can be calculated, applying the PMM procedure, for each MD configuration, providing an ensemble that was used to determine the free energy profile.[51]

RESULTS

During MD simulations, CO molecules, starting from distal pocket (DP), migrate toward the interior of Ngb, populating the internal cavities, or rather escaping into the solvent. Previous crystallographic studies showed that the network of cavities in Ngb is characterized by a huge tunnel, which connects the distal pocket to the rest of the protein matrix.[21,30] Such a tunnel

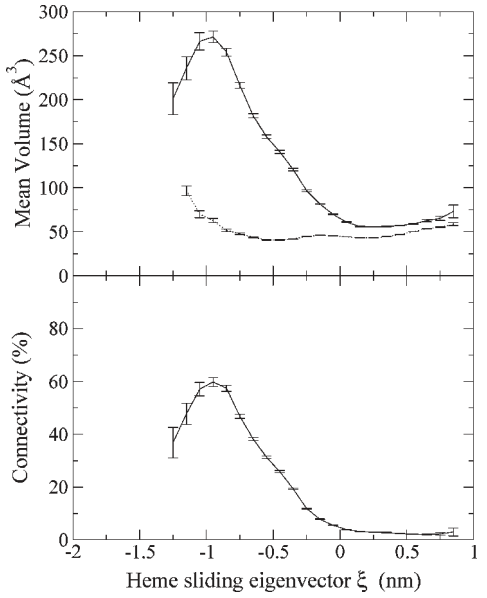

Figure 1. Mean volume of the distal pocket (upper panel) and its connectivity with other cavities (bottom panel) as a function of the heme sliding coordinate. The negative values of abscissa correspond to the heme displaced in the interior of the protein, whereas the positive values indicate heme in more external positions. The mean volumes were calculated considering the configurations in which DP is connected or not connected with other cavities (—) or only not connected (- - -).

exhibits a topological reorganization coupled to the heme sliding,[30] with the proximal branch of the tunnel being occupied by the heme and the distal branch that simultaneously extends on the distal side. To evaluate the influence of the heme position on the DP structure, we analyzed the mean volume of DP and its connectivity with other cavities as a function of the heme sliding reaction coordinate ξ (Figure 1). The heme sliding reaction coordinate was calculated by means of the essential dynamics (ED) analysis, which was performed on all heme atoms with the exception of the terminal propionic chains. The eigenvectors with large eigenvalues correspond to the principal directions on motion of the heme group, and coherently with previous studies[31,32] we chose as heme sliding reaction coordinate the first essential eigenvector obtained by ED analysis performed on carboxy Ngb (NgbCO) in solution[31] where the heme sliding, in the direction from D to B pyrrole ring, was first detected. The configurations in which DP is, directly or indirectly, connected to the solvent were not taken into account for the calculation of mean volumes and connectivity, while the CO ligand contribution was neglected. We consider the mean volumes of DP in two different conditions: when DP was connected or not connected to other cavities (Figure 1, upper panel, —) or when DP was only not connected (- - -). In Figure 1 (bottom panel), the connectivity of DP with other pockets is reported as a function of heme sliding reaction coordinate. The negative values of ξ correspond to the heme displaced in the interior of the protein, whereas positive values indicate heme in more external positions. Coherently with the crystallographic data on tunnel topological reorganization,[30] the connectivity of DP with other pockets is dramatically dependent by the heme sliding. In particular, we observe a connectivity maximum of 60% of simulation time when the heme is in the interior of the protein, whereas the connectivity rapidly decreases to 3% throughout the heme displacement

Table 1. Amino Acids Lining the Internal Cavities in Murine Ngb

Xe1	Xe2	Xe3	Xe4	Ph1
Leu92	Ile72	Ala75	Gly24	Trp13
His96	Tyr137	Leu136	Leu27	Leu113
Phe106	Val140	Val140	Phe28	Met116
Met144			Ile65	Leu117
			Val68	Trp133
			Met69	

toward the surface of Ngb. Accordingly, the DP mean volume follows the same trend. It interesting to note that the effect of the heme sliding on the DP intrinsic volume is less pronounced, as shown by the mean volume values corresponding to DP not connected to other sites (Figure 1, upper panel, - - -). As a consequence of DP topological reorganization with the heme sliding, a reliable study of the diffusion of photolized CO in Ngb should consider several starting configurations with different heme positions and not only a single crystallographic structure, whose exclusive use might introduce a bias. In addition, it is worth noting that previous MD simulations evidenced that the most probable heme position in the crystal environment[32] is in fact marginal in solution.[31] For this purpose, the seven starting coordinates employed for the simulations were taken from the previously performed extended MD simulation of the CO-bound murine Ngb in solution,[31] according to the correct probability distribution, and the initial heme sliding coordinate values ξ_0 were 0.58, 0.02, 0.03, 0.28, −0.04, 0.29, and −0.56 nm, respectively.

In Mb, four small hydrophobic cavities exist.[33] These so-called xenon cavities (from Xe1 to Xe4) were shown to be part of the ligand migration pathway through the protein matrix.[1,4,58−60] Moreover, two additional cavities called phantom1 (Ph1) and phantom2 (Ph2) were detected in Mb by MD simulations.[13] In previous studies on Ngb, it was noted a topological correspondence between the cavities in Mb and those evidenced in Ngb matrix.[31,36,37] In particular, similarities were evidenced with Xe1, Xe2, Xe3, Xe4, and Ph1 (which will be considered herein as included in the adjacent cavity Xe4 for simplicity). The residues lining such cavities in Ngb are reported in Table 1. To shed light on the routes followed by photolized CO molecules during the migration through the Ngb interior, we analyzed the CO transitions between each pair of adjacent cavities. In Table 2, we report the statistical characterization of the transitions involving such cavities. The total number of transitions between cavities i and j ($N_{i,j}$) is reported in Table 2 (column 1). In Table 2 (column 2), the mean relative frequency ($N_{i,j}/\Sigma_j N_{i,j}$) is reported. It represents the number of transitions $i \rightarrow j$ over the total number of transitions starting from a given cavity i. The occurrence (Table 2, column 3) is equal to the fraction of trajectories in which a given transition type $i \rightarrow j$ is observed at least once. Initially, CO molecules migrate from DP to Xe2 or alternatively to Xe4. Both transitions are observed at least once in >70% of trajectories, although the transition to Xe2 is largely more favored (83% of transitions observed from DP). From Xe2, the ligands can migrate back to DP (8% of transitions observed from Xe2) or toward Xe4 (80%), Xe3 (10%), Xe1 (2% of transitions observed from Xe2). From Xe4, the ligands preferentially migrate back to Xe2 (98% of transitions), whereas the return to DP is less probable (2% of transitions). Seldom do CO molecules move

Table 2. Statistical Characterization of the Kinetic Steps Describing the Migration of CO Molecules in Murine Ngb

	total number of transitions	mean relative frequency	occurrence (% of trajectories)
DP→Xe2	1447	0.83	87
DP→Xe4	304	0.17	77
Xe2→DP	1429	0.08	83
Xe2→Xe4	14 590	0.80	84
Xe2→Xe3	1774	0.10	69
Xe2→Xe1	336	0.02	59
Xe4→DP	293	0.02	74
Xe4→Xe2	14 614	0.98	84
Xe4→Xe3	20	>0.01	7
Xe3→Xe2	1773	0.94	70
Xe3→Xe4	29	0.01	11
Xe3→Xe1	94	0.05	24
Xe1→Xe2	327	0.76	60
Xe1→Xe3	103	0.24	30

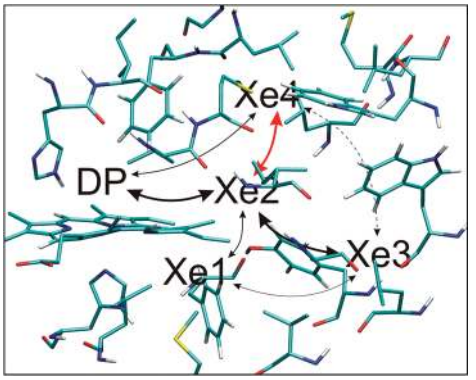

Figure 2. Migration routes followed by photolized CO in Ngb. CO molecules starting from DP migrate into the Xe2 cavity, from which they reach other minor xenon cavities Xe4, Xe3 (thick arrows), or Xe1. A fast interchange between Xe2 and Xe4 is observed (red arrows). Secondary pathways involve an interchange between DP and Xe4 or between Xe3 and Xe1 (thin arrows). Seldom does CO migrate from Xe4 to Xe3 (dashed arrows).

from Xe4 and reach Xe3 via the region corresponding to Ph1 cavity (>0.01%). Moreover, from Xe1 and Xe3, the most probable transitions are those involving the cavity Xe2, whereas the transitions involving other adjacent cavities as extremely rare. Therefore, from data reported in Table 2 (see Figure 2), it is clear that CO molecules starting from DP migrate into Xe2 cavity, from which they reach other minor Xe cavities. It is interesting to note how from this view emerges a pivoting role of the huge, central cavity Xe2 in controlling the migration of the ligand in Ngb. Furthermore, it is worth noting that Xe2, with DP, is the cavity directly involved in the heme sliding.

Within such a definition of the CO sites and considering the connection statistics reported in Table 2, MD data provided the following kinetic scheme (for the moment, we do not include possible escape routes):

$$\mathrm{DP} \rightleftarrows \mathrm{Xe2} \rightleftarrows (\mathrm{Xe4}, \mathrm{Xe3}, \mathrm{Xe1})$$

Analysis of MD data showed that the transitions occurring between Xe2 and Xe4 are very fast, whereas those occurring

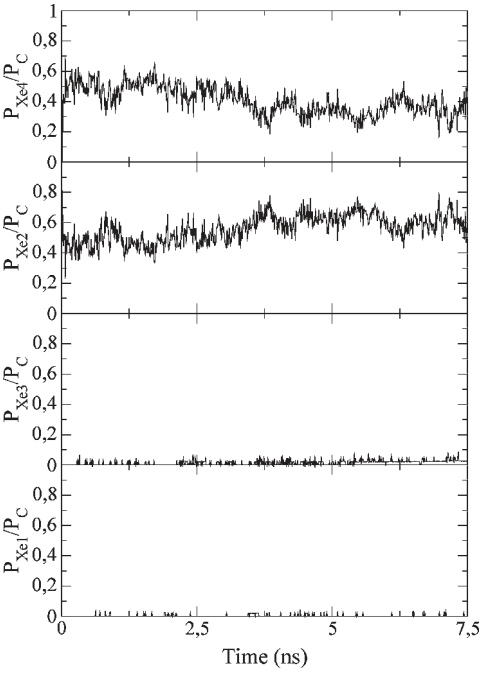

Figure 3. Time dependence of the CO fractions in xenon cavities relative to site C overall probability, as obtained by MD data.

between Xe2 and other cavities as Xe1 or Xe3 are uncommon. This is well illustrated by considering the time dependence of the CO distribution among the Xe cavities, that is, P_{Xe4}/P_C, P_{Xe2}/P_C, P_{Xe3}/P_C, and P_{Xe1}/P_C, with P as the probability of a given CO site and $P_C = P_{Xe1} + P_{Xe2} + P_{Xe3} + P_{Xe4}$, as shown in Figure 3 (we note that the fractions Xe3 and Xe1 are neglible within the noise, indicating that these cavities are used to allow ligand transitions but they are rather unstable CO sites, at least for solvated Ngb). The above scheme may then be simplified by grouping together Xe4, Xe2, Xe3, and Xe1 as a single CO kinetic site C, whose internal distribution is in pre-equilibrium with respect to the other kinetic steps.

$$\mathrm{DP} \underset{k_{-1}}{\overset{k_1}{\rightleftarrows}} \mathrm{C}$$

dx.doi.org/10.1021/jp110833v |J. Phys. Chem. B 2011, 115, 2436–2446

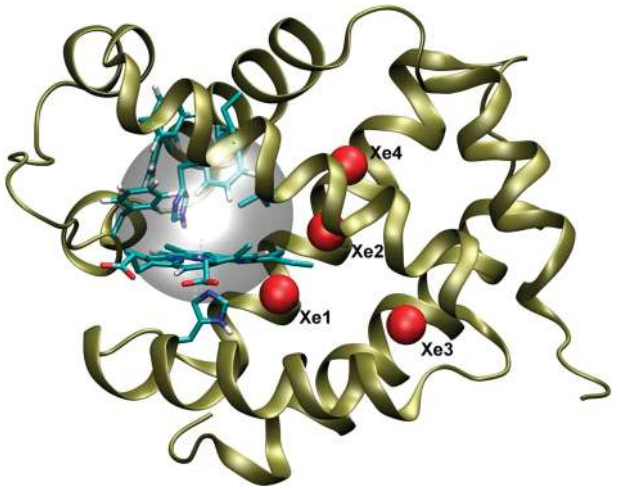

Figure 4. Sample configuration of Ngb as extracted from MD simulations in solution. The heme, distal His64, proximal His96, and other residues lining the distal pocket (gray surface) are depicted by sticks. The positions of the xenon cavities are reported as red spheres.

The simplified kinetic scheme allows us to redefine the criteria used to assign each CO molecule to a given kinetic site. In Figure 4, a model of Ngb is reported. We defined as CO in DP each CO molecule at a distance lower than 6 Å from the geometrical center of DP. The results are insensitive for the cutoff distance ranging from 4 to 6 Å, as such a range corresponds to a hindered region occupied by the residues lining DP. In Figure 4, the corresponding volume is depicted as a delimiting gray surface. The other positions inside Ngb, with the exception of DP, were defined as kinetic site C. Moreover, we include as third kinetic state the CO in solvent, outside Ngb. During MD simulations, CO molecules escape 12 times. In particular, in our simulations (see Figure S1 in the Supporting Information), 8 ligand molecules escaped crossing the Xe4 region corresponding to Ph1 site, between the helix G and the turn connecting A and B helices (residues 16, 23, 26, 27, 116, 120, 121). Such an escape route was evidenced also in human Ngb.[36] Two CO molecules escaped in correspondence of CD corner, either between B and D helices (residues 29, 32, 52, 55, 56) or between the G helix and the loop connecting B and C helices (residues 34, 35, 109, 112), whereas other two CO molecules escape through the region delimited by the BC loop and the FG loop (residues 35, 37, 41, 105, 108). As all 12 escape routes involve cavity C, within our definition of kinetic state we complete the kinetic scheme to be used:

$$\mathrm{DP} \underset{k_{-1}}{\overset{k_1}{\rightleftarrows}} \mathrm{C} \xrightarrow{k_e} \mathrm{Ngb} + \mathrm{CO} \qquad \text{(scheme 1)}$$

where DP indicates the distal pocket, Ngb + CO denotes the free ligand state, which typically may still be considered as virtually irreversible in the microseconds time range, and C represents the ensemble of the Ngb internal cavities.

The last kinetic scheme, governed by three kinetic constants, assumes that within the simulation time range (7.5 ns) a significant CO fraction escapes from the protein and that only CO molecules located in the kinetic site C were able to escape, indicating that other ligand exit sites, although possible, may be considered as secondary exit sites. It is interesting to note that no exit was observed through the so-called histidine gate, a short hydrophobic channel, transiently formed upon the rotation of the His64 side chain around its χ_1 torsional angle, postulated in Mb.[61,62] Such a result might be explained considering that, according to the previous MD simulation in solution, the opening of the histidine gate is coupled to the displacement of E helix to the heme plane that increases the hindrance and obstructs the hydrophobic channel.[31] In addition, it is worth noting that we assumed the same kinetic constant k_e for all CO exit routes. The latter approximation is equivalent to consider the ligands escaping from the huge cavity composed by Xe1, Xe2, Xe3, Xe4 and to suppose almost the same energetic barrier between each cavity gate and the solvent.

Table 3. Phenomenological Kinetic Constants (ns^{-1}) Describing the Migration of CO in Ngb for Trajectories Subsets[a]

	k_1	k_{-1}	k_e
subset 1	1.4	5.5×10^{-1}	4.4×10^{-2}
subset 2	1.7	4.7×10^{-1}	3.6×10^{-2}
std. error	1.1×10^{-1}	2.8×10^{-2}	2.8×10^{-3}

[a] The standard errors for each constant distribution are reported.

According to the migration scheme, we set the system of linear differential equations, parametrically dependent on the three phenomenological rate constants (k_1, k_{-1}, and k_e), whose solution provides the complete relaxation kinetics as described in detail in the Appendix. Solving the system of equations for different sets of the three rate constants, we were able to evaluate their values, which best reproduce the kinetic trace provided by MD simulations. The sets of the three rate constants were chosen in a wide range of real positive parameters, performing a search through a grid of geometrically spaced points. Reducing iteratively the grid spacing, a proper set of constant with a desired approximation was evaluated. Such estimated phenomenological rate constants ($k_1 = 1.5\ ns^{-1}$, $k_{-1} = 5.0 \times 10^{-1}\ ns^{-1}$, $k_e = 4.0 \times 10^{-2}\ ns^{-1}$) for CO intraprotein migration and escape determined the two kinetic eigenvalues ($\lambda_1 = -2.0\ ns^{-1}$, $\lambda_2 = -3.0 \times 10^{-2}\ ns^{-1}$) characterizing the complete ligand migration/escape kinetics.

To evaluate the capability of the time-dependent occupancies derived from 70 MD trajectories to provide a good convergence of the phenomenological kinetic constants, the same procedure was repeated on two different subsets of 35 MD trajectories respectively. Both subsets include five trajectories starting from each of the initial configurations. We report in Table 3 the values of the phenomenological kinetic constants, as obtained from each of two subsets. The standard errors, evaluated by two subsets, are also reported in Table 3 for each kinetic constant. As the average of the two kinetic constants given by the subsets is generally not equal to the corresponding kinetic constant calculated from the whole set of 70 MD trajectories, such standard errors should be considered as a rough, probably overestimated approximation of the inaccuracy that affects the phenomenological kinetic constants.

The obtained kinetic eigenvalues provide two relaxation processes of largely different time scales with $\lambda_1 \approx -(k_1 + k_{-1})$ corresponding to the DP−C ligand exchange relaxation rate and $\lambda_2 \approx -k_e\chi_C = -k_e k_1/(k_1 + k_{-1})$ providing the much slower ligand exit rate as given by a pre-equilibrium CO distribution inside Ngb (χ_C is the equilibrium probability for a CO molecule within Ngb to be located in kinetic site C, which is about 0.75 ±

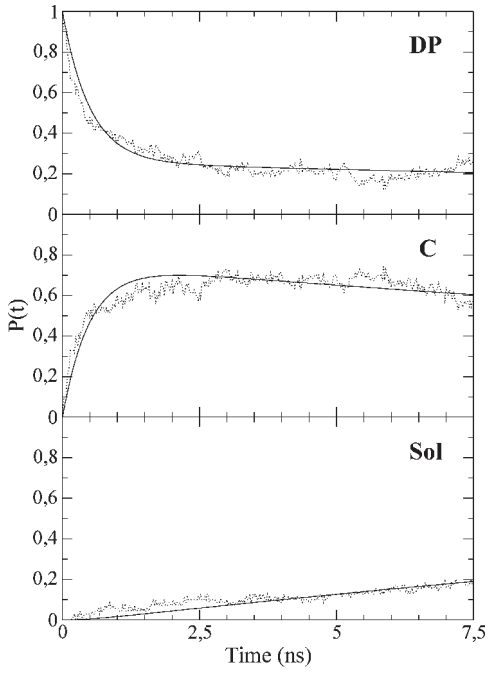

Figure 5. Kinetic trace of photolized CO occupancy (probability) in the three sites (DP, distal pocket; C, hydrophobic internal cavities; Sol, free carbon monoxide in the solvent) considered in the kinetic scheme 1: MD data (· · ·), kinetic model (−).

0.02 from our data). Moreover, we obtained the estimated mean lifetimes for the DP to C transition, $1/k_1 \cong 0.67 \pm 0.05$ ns, and ligand escape, $1/(k_e\chi_C) \cong 33 \pm 3$ ns. The ligand escape from Ngb is 3−6 times faster than the escape rate observed in Mb,[12,52] and the escape route through the histidine gate, on the contrary of Mb, is rare. In addition, also the migration from DP to the interior of Ngb is faster (700 ps) than that observed in Mb (4−5 ns).[52,63] It has to be noted that the ligand migration in Ngb has not been experimentally observed, differently from Mb, and it might be due to the faster diffusion in Ngb. In addition, we can compare the phenomenological kinetic constants with those obtained fitting flash photolysis experimental data measured in solution at 293 K.[64] It should be pointed out that Viappiani and co-workers used a quite different kinetic scheme: from DP the carbon monoxide was able to directly escape into the solvent or sequentially populate four presumed docking sites.[64] In that study, the CO escape rate from Ngb was evaluated to be 1.4×10^{-1} ns^{-1}, whereas the migration from DP to the following docking site and its reverse rate were 5.5×10^{-2} and 1.3×10^{-1} ns^{-1}, respectively.[64] In addition, an extremely fast recombination between CO and heme was observed (1.5×10^{-2} ns^{-1}) with an estimated activation entropy of −107 J/(mol K) and an undetectable activation enthalpy.[64]

In Figure 5, we report the time course of CO occupancy, that is, probability, for Ngb ligand sites (DP, C) and free ligand state (Sol), as obtained by MD simulations and evaluated by the theoretical kinetic model defined by the estimated eigenvalues. The accuracy of the model kinetics to reproduce MD data for all CO states demonstrates the reliability of the simple migration scheme used and the good convergence of the time-dependent occupancies provided by the 70 MD trajectories.

Previously, it was shown that the connectivity between DP and the cavity C is strongly influenced by the heme sliding. Such a result suggests that the kinetics of CO migration in Ngb might be affected by the position of the heme as well. To clarify this question, a study of the CO diffusion should be performed as a function of the position of the heme along the sliding reaction coordinate ξ. Although the heme starts from different position ξ_0, it considerably fluctuates during the simulations, populating several regions. Therefore, the migration of CO in Ngb might be dependent not only on the initial position but also on the instantaneous positions of the heme, kept throughout the simulations. However, the comparison of the phenomenological kinetic constants according to the initial position should be demonstrative of the influence of the heme sliding on the CO migration kinetics. We have obtained 10 independent trajectories from each of the 7 initial configurations characterized by a distinct initial heme position ξ_0. As 10 independent trajectories should provide a sufficient statistics, it is possible to test the convergence for each phenomenological kinetic constant, increasing the number of trajectories used according to the initial heme positions and comparing the results with those provided by a set in which the trajectories are randomly chosen, retaining the correct initial heme position distribution. In Figure 6A, we report the values of each phenomenological kinetic constant (k_1, k_{-1}, k_e) as a function of the number of trajectories considered to build the kinetic model. We considered sets in which the trajectories are progressively ordered and added according to the initial heme position, from the largest to the smallest values of ξ_0 (− − −) or vice versa (− · − · −), or not ordered but randomly chosen (−). From data reported in Figure 6A, it is evident that the convergence of the phenomenological kinetic constants k_1 and k_{-1} is strongly influenced by the choice of the initial heme positions, and the constants do not converge when a biased ξ_0 distribution is considered: k_1 ranges from 22 ns^{-1} (when only trajectories with the smallest values of ξ_0 are considered) to 0.2 ns^{-1} (when only trajectories with the largest values of ξ_0 are considered). In the same way, k_{-1} ranges from 2 to 0.08 ns^{-1}. In general, for smaller values of ξ, corresponding to a high connectivity between DP and cavity C, a fast diffusion from DP (high k_1) is promoted, whereas for larger values of ξ, corresponding to a low connectivity between the two cavities, the migration is slower (low k_1). On the contrary of k_1 and k_{-1}, k_e is substantially insensitive to the initial heme position, confirming that the CO escape routes do not involve regions affected by the heme sliding, but are localized far from DP.

To further validate the influence of the heme sliding on CO migration kinetics, we considered two subsets of 30 trajectories each; the first one (SL−) includes the trajectories starting from the three smallest values of ξ_0, while the other (SL+) includes the trajectories with the three largest ξ_0. For SL−, we obtained $k_1 = 2.8$ ns^{-1}, $k_{-1} = 3.1 \times 10^{-1}$ ns^{-1}, $k_e = 3.6 \times 10^{-2}$ ns^{-1}, while instead for SL+, we obtained $k_1 = 4.4 \times 10^{-1}$ ns^{-1}, $k_{-1} = 3.0 \times 10^{-1}$ ns^{-1}, $k_e = 4.2 \times 10^{-2}$ ns^{-1}. The time course of CO occupancies as evaluated by the kinetic model is reported in Figure 6B for SL+ (−) and SL− (− − −). It is worth noting that the differences in the number of CO escaped in each subset are more due to the different fraction of photolized ligands in C, χ_C, than to k_e variation.

Although the migration of CO in Ngb allowed us to define several potential docking sites, some of them are unstable sites. Moreover, a given complex kinetic scheme may be reduced to a simple equilibrium between DP and a single huge cavity C. These results indicate that the energy barrier, to be overcome, between DP and the cavity C is significantly higher than the energy

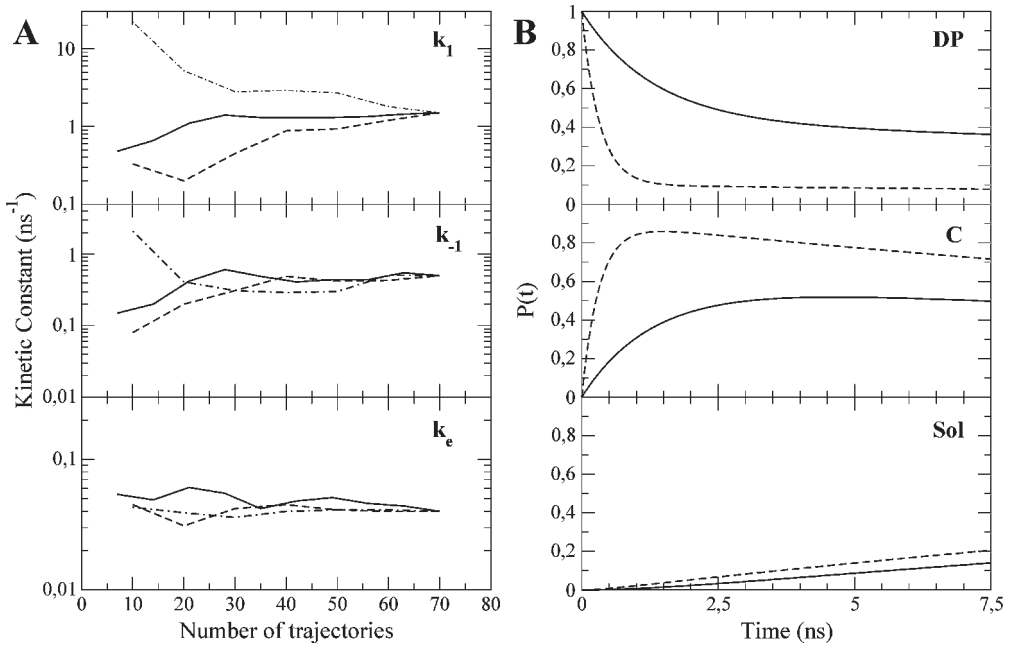

Figure 6. (A) Phenomenological kinetic constants (k_1, k_{-1}, k_e) as a function of the number of trajectories considered to build the kinetic model: trajectories are progressively ordered and added according the initial heme position (ξ_0), from the largest to the smallest values of ξ_0 (− − −) or vice versa (− · − · −), or not ordered but randomly chosen (−). (B) Kinetic trace of photolized CO occupancy (probability) in the three sites (DP, distal pocket; C, hydrophobic internal cavities; Sol, free carbon monoxide in the solvent) considered in the kinetic scheme 1: subset SL+ (−), subset SL− (− − −).

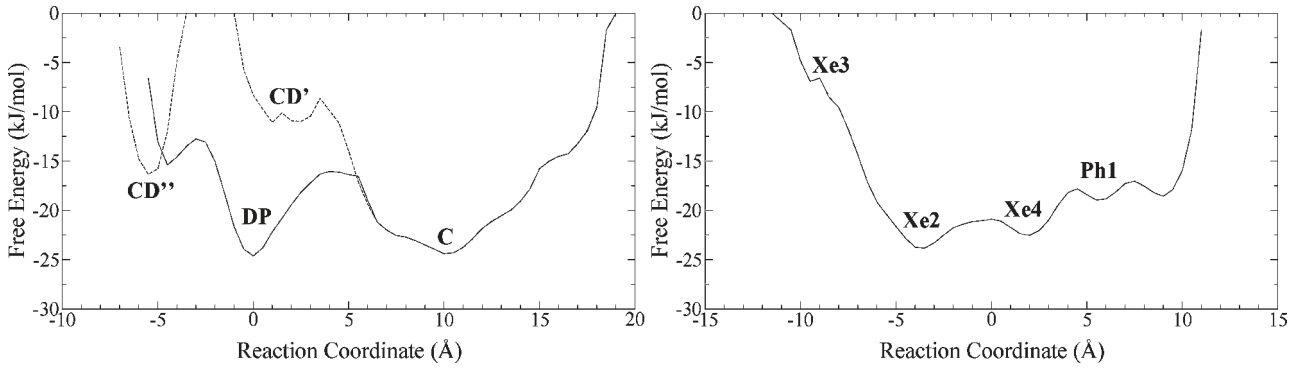

Figure 7. Carbon monoxide free energy landscapes: (left panel) from DP to C site (the abscissa indicates the distance from the center of the distal pocket, while the dashed line represents the CO free energy landscape inside site C along the reaction coordinate connecting DP to site C); (right panel) from Xe2 to Xe4 cavity (the solid line represents the CO free energy landscape inside site C along the reaction coordinate connecting Xe2 to Xe4).

barriers between two adjacent pockets belonging to cavity C. To verify such a feature, we calculated two free energy landscapes, via equilibrium distribution of the ligand center of mass projections along two reaction coordinates, representing roughly the diffusion directions of CO molecules inside Ngb.

In Figure 7 (left panel), we report the free energy landscapes along the direction axis connecting the DP geometrical center to the middle point between the Xe4 and Xe2 geometrical centers. The DP geometrical center was used as a reference point. We considered two free energy landscapes provided by two distinct subsets, to remove overlaps due to having represented a three-dimensional distribution as a one-dimensional projection distribution along a reaction coordinate. The first subset includes the configurations with CO inside DP (projection values ranging from −6 to 6 Å) and the configurations with CO inside C with a projection value along the coordinate axis larger than 6 Å (−). The second subset includes only all configurations with CO inside C (dashed line). In addition to DP and C sites are evident two relatively unstable docking sites (dashed line) at projection values of 2 and −5.5 Å, which correspond to two sites in CD corner (CD′, CD″) that are somewhat populated by CO molecules that eventually escape into the solvent. CD′ is in the region delimited by residues Leu56, Phe61, and the B helix, whereas CD″ is delimited by Phe42, Tyr44, Phe49, Phe61, and His64 and may be accessed only from DP. It is worth noting that some analogies exist between the CD docking sites and some cavities detected in previous computational studies.[37] A free energy barrier of ∼8 kJ/mol is between DP and site C, while CD′ and CD″ free energy minima are, respectively, 14 and 8 kJ/mol less stable than those observed for DP and site C.

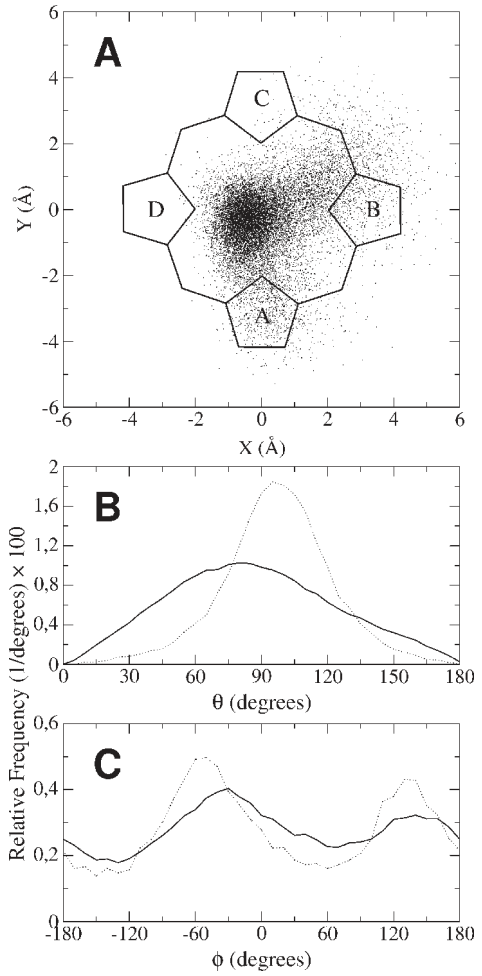

Figure 8. Projection of the CO center of mass onto the heme plane (A) in Ngb, as detected in the MD simulations. Probability distributions for the orientation angles θ (B) and ϕ (C) (see text). The distributions for the angles θ and ϕ are reported for Ngb (—) and Mb (- - -).

In Figure 7 (right panel), we report the free energy landscape along the direction axis connecting the Xe2 and Xe4 geometrical centers. We considered a free energy landscape provided by projecting all configurations with CO inside C along the reaction coordinate. From the free energy profile, five free energy minima may be noted at −9.5, −3.5, 2.0, 5.5, 9.0 Å, corresponding to free energies of −7.0, −24.0, −22.5, −19.0, −18.5 kJ/mol. The first four sites correspond to Xe3, Xe2, Xe4, Ph1 cavities, respectively, whereas the last site represents several temporary docking sites on the protein surface populated by CO molecules during their migration into the solvent. Moreover, it is worth noting that the free energy barriers between Xe2 and Xe4 are quite lower than that observed between DP and Xe cavities, ranging from 2.0 to 3.2 kJ/mol.

In Mb, the CO ligand resides immediately after photolysis in primary docking site above heme pyrrole ring C, at about 4.5 Å from iron, parallel to the heme plane, and it principally adopts two antiparallel orientations, respectively, with the carbon or the oxygen atom pointing back toward the iron.[2,58,60,65] To describe the position and the orientation of the CO molecule in Ngb distal pocket and compare the results with those collected in Mb, we consider both the projection of the CO geometrical center onto the heme plane and the two polar angles θ and ϕ: the first is

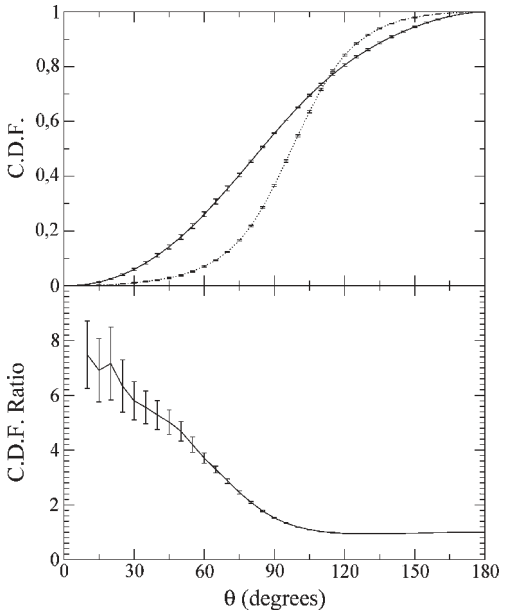

Figure 9. Cumulative distribution functions (c.d.f.) calculated from the distribution of the θ angle (upper panel) for Ngb (—) and Mb (- - -). Ratio between the cumulative distribution function of Ngb and Mb (bottom panel).

defined as the angle between the normal to the heme plane and the bond vector oriented from the carbon to the oxygen atom (C→O) of the ligand, the second is the angle between the projection of the C→O bond vector onto the heme plane and the vector Fe→N_C, connecting the heme iron to the nitrogen atom of the pyrrole ring C. In Figure 8A, the distribution of the geometrical center projection onto heme plane is reported. Interestingly, in the distal pocket, the ligands do not populate predominantly a region corresponding to the primary docking site, found in Mb, but instead the CO molecules reside above the iron at a distance of 3.8 Å. Moreover, the distributions of the θ (Figure 8B) and ϕ (Figure 8C) angles show that the CO ligand is parallel to the heme plane and adopts two antiparallel orientations analogously to Mb distal pocket, but the distributions are less peaked, evidencing a structural disorder. In Figure 9 (upper panel), the cumulative distribution functions (c.d.f.) calculated from the distribution of θ angle for Ngb (—) and Mb (- - -) are reported. It is evident in Ngb an increase of the probability of orientations with the carbon atom facing the heme iron, which might promote the ligand recombination. The ratio between the two cumulative distribution functions (Figure 9, bottom panel) evidences that the probability to find CO molecules with a small value of θ angle is 6−8 times higher than in Mb.

In previous papers,[51,52] a quantitative description of the reaction free energy and related kinetics for the CO−heme bond formation−disruption in solvated Mb was obtained, by means of PMM calculations[51] on the CO−heme covalent complex along the reaction coordinate (carbon−iron distance, i.e., the length of the carbon−iron connecting vector). Herein, combining the reaction free energy in the 0.18−0.38 nm reaction coordinate range, as obtained by PMM, with the free-energy variation along the carbon−iron distance, beyond 0.38 nm, provided by the unbound CO diffusion within the distal pocket, as obtained by the present MD simulations (i.e., via the equilibrium distribution), we can evaluate the free-energy profile for the

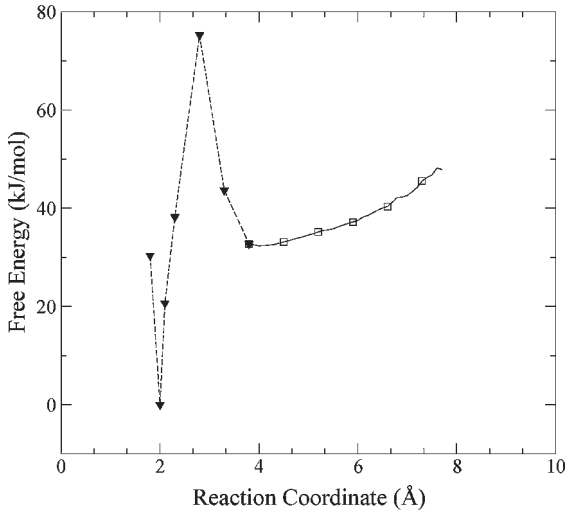

Figure 10. Free energy profile (within distal pocket) along the CO−heme reaction coordinate (carbon−iron distance) as obtained by MD/PMM calculations.

complete binding−unbinding reaction step for carbon monoxide in Ngb, as shown in Figure 10.

Hence, using the kinetic model on the basis of solving a Fokker−Planck equation for the diffusion process on the reaction free-energy surface and extracting from the solution the rate constants for the reactant−product conversion, we may express the kinetics for the binding−unbinding process via

$$\mathrm{NgbCO} \underset{K_{bin}}{\overset{K_{unb}}{\rightleftarrows}} \mathrm{DP}$$

$$\dot{P}_{NgbCO} = -K_{unb}P_{NgbCO} + K_{bin}P_{DP}$$

with NgbCO as the CO−heme bound state, P_{NgbCO} as the corresponding probability, and K_{unb} and K_{bin} as the rate constants for the unbinding and binding, respectively. Note that in the above binding−unbinding reaction scheme, the coupled rate equations for P_{NgbCO} and P_{DP} follow from the steady-state approximation for the transition-state (TS) probability. Note also that $K_{unb} = \kappa \exp(-\beta\Delta\mu_{NgbCO}^{\#})$ and $K_{bin} = \kappa \exp(-\beta\Delta\mu_{DP}^{\#})$, where κ is a weakly temperature-dependent factor (herein $\kappa = 20\ \mathrm{ps}^{-1}$),[52] given by the microscopic rate constants for TS → NgbCO and TS → DP transitions, providing the transition rate in the limit of ideal barrierless conditions, $\Delta\mu^{\#} = \Delta A^{\#}$ is the activation (Helmholtz) free energy,[51] that is, variation of the standard chemical potential between the TS and the NgbCO or DP state, and $1/\beta = k_B T$, with k_B as the Boltzmann constant and T as the absolute temperature. The reaction free energy profile shown in Figure 10 provides $\Delta\mu_{NgbCo}^{\#} = 75$ kJ/mol and $\Delta\mu_{DP}^{\#} = 47$ kJ/mol (standard errors ∼1 kJ/mol), resulting in $K_{unb} = 0.84\ \mathrm{s}^{-1}$ and $K_{bin} = 0.088\ \mu\mathrm{s}^{-1}$, corresponding to mean lifetimes of about 1 s and 11 μs, respectively, rather close to the corresponding values provided by analogous calculations performed in Mb.[52]

The obtained binding−unbinding rate constants (K_{bin} and K_{unb}) providing relaxation kinetics in the microseconds and seconds range, respectively, clearly indicate that the CO distribution inside of Ngb, occurring with a relaxation mean lifetime of few nanoseconds, may be considered as instantaneously equilibrated during the binding−unbinding kinetic step, similarly to CO escape, hence allowing the use of the noncovalent complex Ngb/CO in the binding−unbinding reaction scheme:

$$\mathrm{NgbCO} \underset{\chi_{DP}K_{bin}}{\overset{K_{unb}}{\rightleftarrows}} \mathrm{Ngb/CO} \xrightarrow{\chi_C k_e} \mathrm{Ngb} + \mathrm{CO}$$

The previous scheme provides the estimation[52,66] of the fraction of CO involved in geminate recombination $\chi_{gem} = \chi_{DP}K_{bin}/(\chi_{DP}K_{bin} + \chi_C k_e) = 0.1\%$ and the value of the constant describing the geminate (Ngb/CO population) relaxation kinetics $\chi_{gem} = \chi_{DP}K_{bin} + \chi_C k_e$ with $1/K_{gem} = 33$ ns.

CONCLUSIONS

In this Article, the combined use of MD simulations and quantum mechanical calculations (PMM) allowed the construction of a detailed kinetic model for room temperature CO binding, migration, and escape in solvated murine Ngb.

Our computational study shows an interesting correlation between the heme sliding and the connectivity of the network of internal hydrophobic cavities inside Ngb. In particular, the distal pocket is more connected to other cavities when the heme slides to the interior of the protein, whereas the connection is lower when the heme occupies a more external position in proximity of the protein surface. Such features are in agreement with the previously observed topological rearrangements of the cavities coupled to the heme sliding mechanism. Moreover, these results indicate the requirement to use several starting configurations, resembling a correct distribution of the heme positions in solution, to perform an unbiased study of the migration kinetics of photolized CO in solvated Ngb. MD simulations show that during the migration CO molecules explore several docking sites. Among these, DP and four internal hydrophobic cavities topologically similar to Xe cavities found in myoglobin might be mentioned. Principally, CO molecules migrate from DP to Xe2 cavity and then reach other sites. However, kinetic data show that the Xe cavities may be considered as a single huge cavity, called C in this Article, in equilibrium with DP. Such a result follows by the fact that the exchange of CO molecules between adjacent cavities, belong to C cavity, is extremely faster than the CO molecules exchange between DP and cavity C. This feature is confirmed also by the free energy profiles that show an energy barrier, between DP and cavity C, 5−6 kJ/mol higher than those between adjacent cavities included in C. The use of a simplified kinetic model allowed us to determine the phenomenological kinetic constants controlling the migration of CO in Ngb and its escape into the solvent, whereas MD simulations combined with quantum mechanical calculations provided the complete free energy profile of the binding−unbinding kinetics of CO at the heme sixth coordination position. The binding−unbinding constants are close to that observed in analogous study performed on myoglobin, suggesting that the effect of the microenvironment provided by the apoprotein around its prosthetic group is not dissimilar from that observed in other globins. Furthermore, structural analysis on the position and orientation of photolized CO in DP evidences a structural disorder. CO molecules do not occupy an analogous primary docking site as in Mb; instead, photolized CO resides just above the iron atom at a distance of 3.8 Å, and configurations with CO molecule perpendicular to heme plane are more common, although the data show a preference for parallel or antiparallel orientation.

Finally, our data show an interesting correlation between the heme position and the phenomenological rate controlling the

ligand migration from DP to cavity C. Apart from being important to provide and unbiased statistics in a computational study, such a correlation might be crucial in comparing the results provided by experimental observations performed on ligand migration in Ngb in different conditions. In fact, the heme position distribution might be affected not only by the medium (solution or crystal),[32] but also by other factors such as temperature or residues substitution.[67] With respect to Mb, where the heme sliding mechanism does not occur, it may be indispensable for providing a correct kinetic model in Ngb to consider the perturbations on the heme position, besides the effects that may directly involve the ligand diffusion.

Several hypotheses might be raised about the role of the heme sliding mechanism and the huge internal cavity in Ngb. Among others, the huge tunnel might be part of a pathway for ligands through the protein matrix connecting the heme iron to the exterior, providing a complementary or alternative route to histidine gate. MD simulations confirm that the ligands principally escape via the huge internal cavity while the distal histidine is involved in a mechanism that is coupled to the motion of the CD corner.[31] Moreover, the capability of the distal histidine to act as an endogenous ligand enhances the heme redox reactivity,[68,69] but also represents a barrier to ligand binding. When the heme sliding was discovered, it was proposed that such a mechanism might have been selected by evolution to facilitate the ligand access to the sixth coordination position.[30] Our study shows that the heme sliding significantly affects the diffusion of the ligand inside Ngb and modulates the ligand distribution between DP and other sites.

APPENDIX

According to the migration kinetic scheme (see Results), we may set the system of differential rate equations providing the kinetics (probability time dependence) of the two relevant CO states within Ngb (DP and C, see Results):

$$\begin{cases} \dot{P}_{DP} = -k_1 P_{DP} + k_{-1} P_C \\ \dot{P}_C = k_1 P_{DP} - (k_{-1} + k_e) P_C \end{cases} \quad (1)$$

with P_{DP} and P_C as the corresponding probabilities, which may be expressed by the more compact matrix equation $\dot{\mathbf{P}} = \tilde{\mathbf{K}}\mathbf{P}$, where

$$\tilde{\mathbf{K}} \equiv \begin{bmatrix} -k_1 & k_{-1} \\ k_1 & -(k_{-1} + k_e) \end{bmatrix} \quad \mathbf{P} \equiv \begin{bmatrix} P_{DP} \\ P_C \end{bmatrix}$$

$$\dot{\mathbf{P}} \equiv \begin{bmatrix} \dot{P}_{DP} \\ \dot{P}_C \end{bmatrix}$$

Introducing the linear transformation that diagonalizes the kinetic matrix, defined by the eigenvectors of, we may readily obtain:

$$\mathbf{P}(t) = \tilde{\mathbf{T}} \begin{bmatrix} e^{\lambda_1 t} & 0 \\ 0 & e^{\lambda_2 t} \end{bmatrix} \tilde{\mathbf{T}}^{-1} \mathbf{P}(0) \quad (2)$$

where λ_1, λ_2 are the kinetic matrix eigenvalues. Finally, from eq 2 we can obtain the probability time dependence for each kinetic state in the migration scheme, including the one for the free ligand state via the relation $P_{Ngb+CO} = 1 - P_{DP} - P_C$.

ASSOCIATED CONTENT

Supporting Information. CO escape routes from neuroglobin into the solvent. This material is available free of charge via the Internet at http://pubs.acs.org.

AUTHOR INFORMATION

Corresponding Author

*Tel.: +39.06.4991.3178. Fax: +39.06.490324. E-mail: m.anselmi@caspur.it.

ACKNOWLEDGMENT

This work was supported by the Italian PRIN Project no. 20074TJ3ZB_002 "Structure and dynamics of redox proteins: theoretical and computational approach" founded by MIUR. We also acknowledge the University of Rome "La Sapienza" for financial support with the Project no. C26A09JKNF and CASPUR (Consorzio interuniversitario per le Applicazioni di Supercalcolo Per Università e Ricerca) for the use of its computational facilities.

REFERENCES

(1) Schmidt, M.; Nienhaus, K.; Pahl, R.; Krasselt, A.; Anderson, S.; Parak, F.; Nienhaus, G. U.; Srajer, V. *Proc. Natl. Acad. Sci. U.S.A.* **2005**, *102*, 11704.

(2) Srajer, V.; Teng, T.; Ursby, T.; Pradervand, C.; Ren, Z.; Adachi, S.; Schildkamp, W.; Bourgeois, D.; Wulff, M.; Moffat, K. *Science* **1996**, *274*, 1726.

(3) Bourgeois, D.; Vallone, B.; Arcovito, A.; Sciara, G.; Schotte, F.; Anfinrud, P. A.; Brunori, M. *Proc. Natl. Acad. Sci. U.S.A.* **2006**, *103*, 4924.

(4) Schotte, F.; Lim, M.; Jackson, T. A.; Smirnov, A. V.; Soman, J.; Olson, J. S.; Phillips, G. N., Jr.; Wulff, M.; Anfinrud, P. A. *Science* **2003**, *300*, 1944.

(5) Srajer, V.; Ren, Z.; Teng, T. Y.; Schmidt, M.; Ursby, T.; Bourgeois, D.; Pradervand, C.; Schildkamp, W.; Wulff, M.; Moffat, K. *Biochemistry* **2001**, *40*, 13802.

(6) Nienhaus, K.; Deng, P.; Kriegl, J. M.; Nienhaus, G. U. *Biochemistry* **2003**, *42*, 9647.

(7) Nienhaus, K.; Deng, P.; Olson, J. S.; Warren, J. J.; Nienhaus, G. U. *J. Biol. Chem.* **2003**, *278*, 42532.

(8) Lim, M.; Jackson, T. A.; Anfinrud, P. A. *Science* **1995**, *269*, 962.

(9) Lim, M.; Jackson, T. A.; Anfinrud, P. A. *Nat. Struct. Biol.* **1997**, *4*, 209.

(10) Scott, E. E.; Gibson, Q. H.; Olson, J. S. *J. Biol. Chem.* **2001**, *276*, 5177.

(11) Gibson, Q. H.; Regan, R.; Elber, R.; Olson, J. S.; Carver, T. E. *J. Biol. Chem.* **1992**, *267*, 22022.

(12) Ruscio, J. Z.; Kumar, D.; Shukla, M.; Prisant, M. G.; Murali, T. M.; Onufriev, A. V. *Proc. Natl. Acad. Sci. U.S.A.* **2008**, *105*, 9204.

(13) Bossa, C.; Anselmi, M.; Roccatano, D.; Amadei, A.; Vallone, B.; Brunori, M.; Di Nola, A. *Biophys. J.* **2004**, *86*, 3855.

(14) Cohen, J.; Arkhipov, A.; Braun, R.; Schulten, K. *Biophys. J.* **2006**, *91*, 1844.

(15) Anselmi, M.; Di Nola, A.; Amadei, A. *Biophys. J.* **2008**, *94*, 4277.

(16) Nutt, D. R.; Meuwly, M. *Biophys. J.* **2003**, *85*, 3612.

(17) Nutt, D. R.; Meuwly, M. *Proc. Natl. Acad. Sci. U.S.A.* **2004**, *101*, 5998.

(18) Hummer, G.; Schotte, F.; Anfinrud, P. A. *Proc. Natl. Acad. Sci. U.S.A.* **2004**, *101*, 15330.

(19) Burmester, T.; Weich, B.; Reinhardt, S.; Hankeln, T. *Nature* **2000**, *407*, 520.

(20) Pesce, A.; Dewilde, S.; Nardini, M.; Moens, L.; Ascenzi, P.; Hankeln, T.; Burmester, T.; Bolognesi, M. *Structure* **2003**, *11*, 1087.

(21) Vallone, B.; Nienhaus, K.; Brunori, M.; Nienhaus, G. U. *Proteins* **2004**, *56*, 85.
(22) Dewilde, S.; Kiger, L.; Burmester, T.; Hankeln, T.; Baudin-Creuza, V.; Aerts, T.; Marden, M. C.; Caubergs, R.; Moens, L. *J. Biol. Chem.* **2001**, *276*, 38949.
(23) Nienhaus, K.; Kriegl, J. M.; Nienhaus, G. U. *J. Biol. Chem.* **2004**, *279*, 22944.
(24) Sun, Y.; Jin, K.; Mao, X. O.; Zhu, Y.; Greenberg, D. A. *Proc. Natl. Acad. Sci. U.S.A.* **2001**, *98*, 15306.
(25) Sun, Y.; Jin, K.; Peel, A.; Mao, X. O.; Xie, L.; Greenberg, D. A. *Proc. Natl. Acad. Sci. U.S.A.* **2003**, *100*, 3497.
(26) Kitatsuji, C.; Kurogochi, M.; Nishimura, S.; Ishimori, K.; Wakasugi, K. *J. Mol. Biol.* **2007**, *368*, 150.
(27) Wakasugi, K.; Morishima, I. *Biochemistry* **2005**, *44*, 2943.
(28) Wakasugi, K.; Nakano, T.; Morishima, I. *J. Biol. Chem.* **2003**, *278*, 36505.
(29) Raychaudhuri, S.; Skommer, J.; Henty, K.; Birch, N.; Brittain, T. *Apoptosis* **2010**, *15*, 401.
(30) Vallone, B.; Nienhaus, K.; Matthes, A.; Brunori, M.; Nienhaus, G. U. *Proc. Natl. Acad. Sci. U.S.A.* **2004**, *101*, 17351.
(31) Anselmi, M.; Brunori, M.; Vallone, B.; Di Nola, A. *Biophys. J.* **2007**, *93*, 434.
(32) Anselmi, M.; Brunori, M.; Vallone, B.; Di Nola, A. *Biophys. J.* **2008**, *95*, 4157.
(33) Tilton, R. F., Jr.; Kuntz, I. D., Jr.; Petsko, G. A. *Biochemistry* **1984**, *23*, 2849.
(34) Moschetti, T.; Mueller, U.; Schulze, J.; Brunori, M.; Vallone, B. *Biophys. J.* **2009**, *97*, 1700.
(35) Orlowski, S.; Nowak, W. *Biosystems* **2008**, *94*, 263.
(36) Bocahut, A.; Bernad, S.; Sebban, P.; Sacquin-Mora, S. *J. Phys. Chem. B* **2009**, *113*, 16257.
(37) Lutz, S.; Nienhaus, K.; Nienhaus, G. U.; Meuwly, M. *J. Phys. Chem. B* **2009**, *113*, 15334.
(38) Kriegl, J. M.; Bhattacharyya, A. J.; Nienhaus, K.; Deng, P.; Minkow, O.; Nienhaus, G. U. *Proc. Natl. Acad. Sci. U.S.A.* **2002**, *99*, 7992.
(39) Vitkup, D.; Petsko, G. A.; Karplus, M. *Nat. Struct. Biol.* **1997**, *4*, 202.
(40) Straub, J. E.; Karplus, M. *Chem. Phys.* **1991**, *158*, 221.
(41) Plattner, N.; Meuwly, M. *Biophys. J.* **2008**, *94*, 2505.
(42) Berendsen, H. J. C.; van der Spoel, D.; van Drunen, R. *Comput. Phys. Commun.* **1995**, *91*, 43.
(43) van Gunsteren, W. F.; Billeter, S.; Eising, A.; Hunenberger, P.; Kruger, P.; Mark, A. E.; Scott, W.; Tironi, I. *Biomolecular Simulations: The GROMOS96 Manual and User Guide*; University of Groningen: Zurich, 1996.
(44) Hess, B.; Bekker, H.; Berendsen, H. J. C.; Fraaije, J. G. E. M. *J. Comput. Chem.* **1997**, *18*, 1463.
(45) Amadei, A.; Chillemi, G.; Ceruso, M. A.; Grottesi, A.; Di Nola, A. *J. Chem. Phys.* **2000**, *112*, 9.
(46) Brown, D.; Clarke, J. H. R. *Mol. Phys.* **1984**, *51*, 1243.
(47) Darden, T.; York, D.; Pedersen, L. *J. Chem. Phys.* **1993**, *98*, 10089.
(48) Essmann, U.; Perera, L.; Berkowitz, M. L.; Darden, T.; Lee, H.; Pedersen, L. G. *J. Chem. Phys.* **1995**, *103*, 8577.
(49) Amadei, A.; Linssen, A. B.; Berendsen, H. J. C. *Proteins* **1993**, *17*, 412.
(50) Laskowski, R. A. *J. Mol. Graphics* **1995**, *13*, 323.
(51) Amadei, A.; D'Abramo, M.; Daidone, I.; D'Alessandro, M.; Di Nola, A.; Aschi, M. *Theor. Chem. Acc.* **2007**, *117*, 637.
(52) D'Abramo, M.; Di Nola, A.; Amadei, A. *J. Phys. Chem. B* **2009**, *113*, 16346.
(53) Aschi, M.; Spezia, R.; Di Nola, A.; Amadei, A. *Chem. Phys. Lett.* **2001**, *344*, 374.
(54) Spezia, R.; Aschi, M.; Di Nola, A.; Amadei, A. *Chem. Phys. Lett.* **2002**, *365*, 450.
(55) Ming, X.; Fang, W. H. *J. Phys. Chem. B* **2008**, *112*, 990.
(56) Li, J.; Ai, Y. J.; Xie, Z. Z.; Fang, W. H. *J. Phys. Chem. B* **2008**, *112*, 8715.
(57) Amadei, A.; D'Alessandro, M.; Aschi, M. *J. Phys. Chem. B* **2004**, *108*, 16250.
(58) Hartmann, H.; Zinser, S.; Komninos, P.; Schneider, R. T.; Nienhaus, G. U.; Parak, F. *Proc. Natl. Acad. Sci. U.S.A.* **1996**, *93*, 7013.
(59) Ostermann, A.; Waschipky, R.; Parak, F.; Nienhaus, G. U. *Nature* **2000**, *404*, 205.
(60) Schlichting, I.; Berendzen, J.; Phillips, G. N., Jr.; Sweet, R. M. *Nature* **1994**, *371*, 808.
(61) Johnson, K. A.; Olson, J. S.; Phillips, G. N., Jr. *J. Mol. Biol.* **1989**, *207*, 459.
(62) Perutz, M. F.; Mathews, F. S. *J. Mol. Biol.* **1966**, *21*, 199.
(63) Anselmi, M.; Aschi, M.; Di Nola, A.; Amadei, A. *Biophys. J.* **2007**, *92*, 3442.
(64) Abbruzzetti, S.; Faggiano, S.; Bruno, S.; Spyrakis, F.; Mozzarelli, A.; Dewilde, S.; Moens, L.; Viappiani, C. *Proc. Natl. Acad. Sci. U.S.A.* **2009**, *106*, 18984.
(65) Teng, T. Y.; Srajer, V.; Moffat, K. *Nat. Struct. Biol.* **1994**, *1*, 701.
(66) Henry, E. R.; Sommer, J. H.; Hofrichter, J.; Eaton, W. A. *J. Mol. Biol.* **1983**, *166*, 443.
(67) Xu, J.; Yin, G.; Du, W. *Proteins* **2011**, *79*, 191.
(68) Weiland, T. R.; Kundu, S.; Trent, J. T., III; Hoy, J. A.; Hargrove, M. S. *J. Am. Chem. Soc.* **2004**, *126*, 11930.
(69) Arcovito, A.; Moschetti, T.; D'Angelo, P.; Mancini, G.; Vallone, B.; Brunori, M.; Della Longa, S. *Arch. Biochem. Biophys.* **2008**, *475*, 7.